

Supporting Information:

Active site engineering in UiO-66 type Metal Organic Frameworks by intentional creation of defects: A theoretical rationalization

Matthias Vandichel,^{a,*} Julianna Hajek,^a Frederik Vermoortele,^b Michel Waroquier,^a Dirk E. De Vos,^b Veronique Van Speybroeck^{a,*}

Contents

1. $Zr_6O_4(OH)_4$ seen from different viewpoints	2
2. Computational Methodology: static periodic calculations	4
3. Figure S.4: Overview of reactions during synthesis	6
4. Figure S.5: Overview of reactions during post-synthesis activation.	7
5. Computational Methodology: Periodic Molecular Dynamics simulations and Nudged Elastic Band calculations to unravel reaction path for dehydroxylation.	8
6. Computational Methodology: Cluster Calculations	9
7. Computational Methodology: extended Hirshfeld-e charges	15

1. $Zr_6O_4(OH)_4$ seen from different viewpoints

Different positioning of the hydroxyl groups, lead to different viewpoints (cfr. Figure 1 and 2).

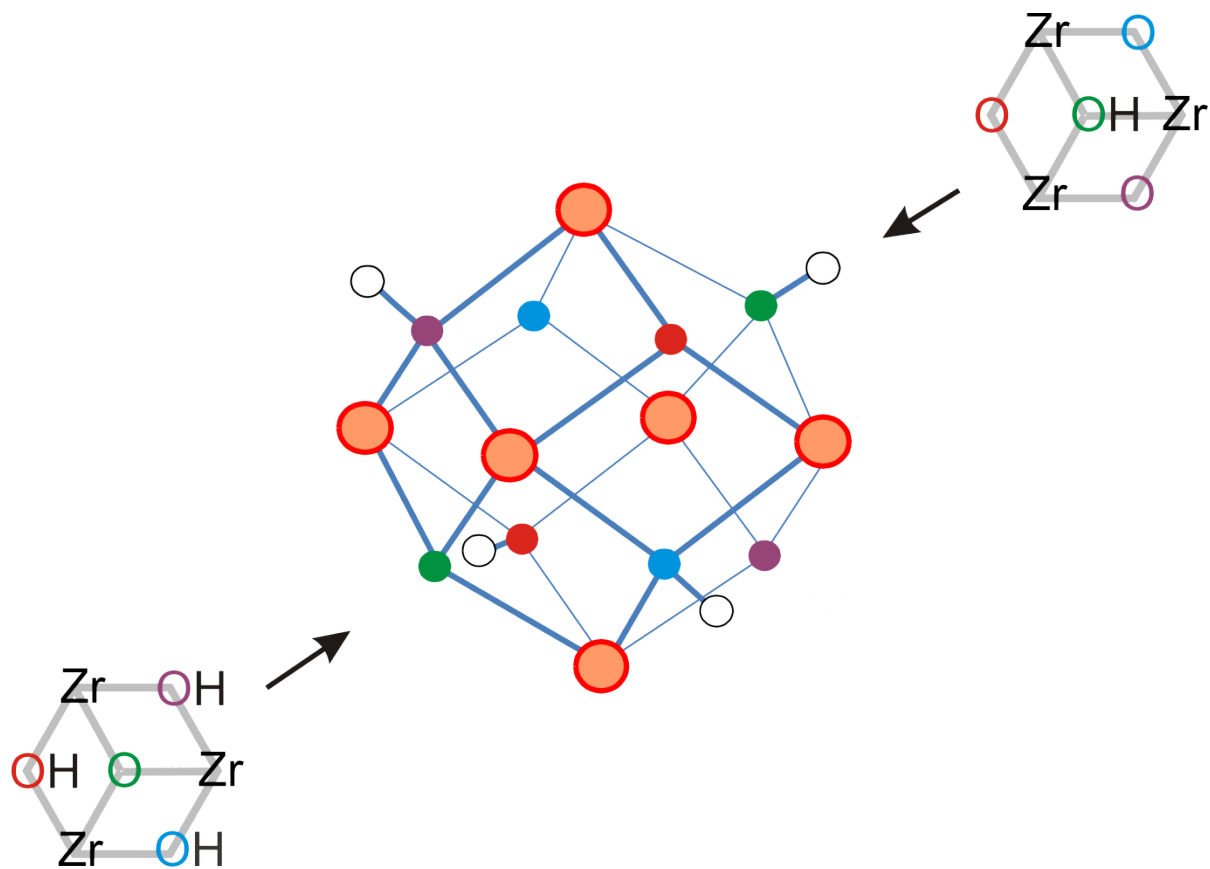


Figure S1: Tetrahedral positioning of the hydrogen atoms

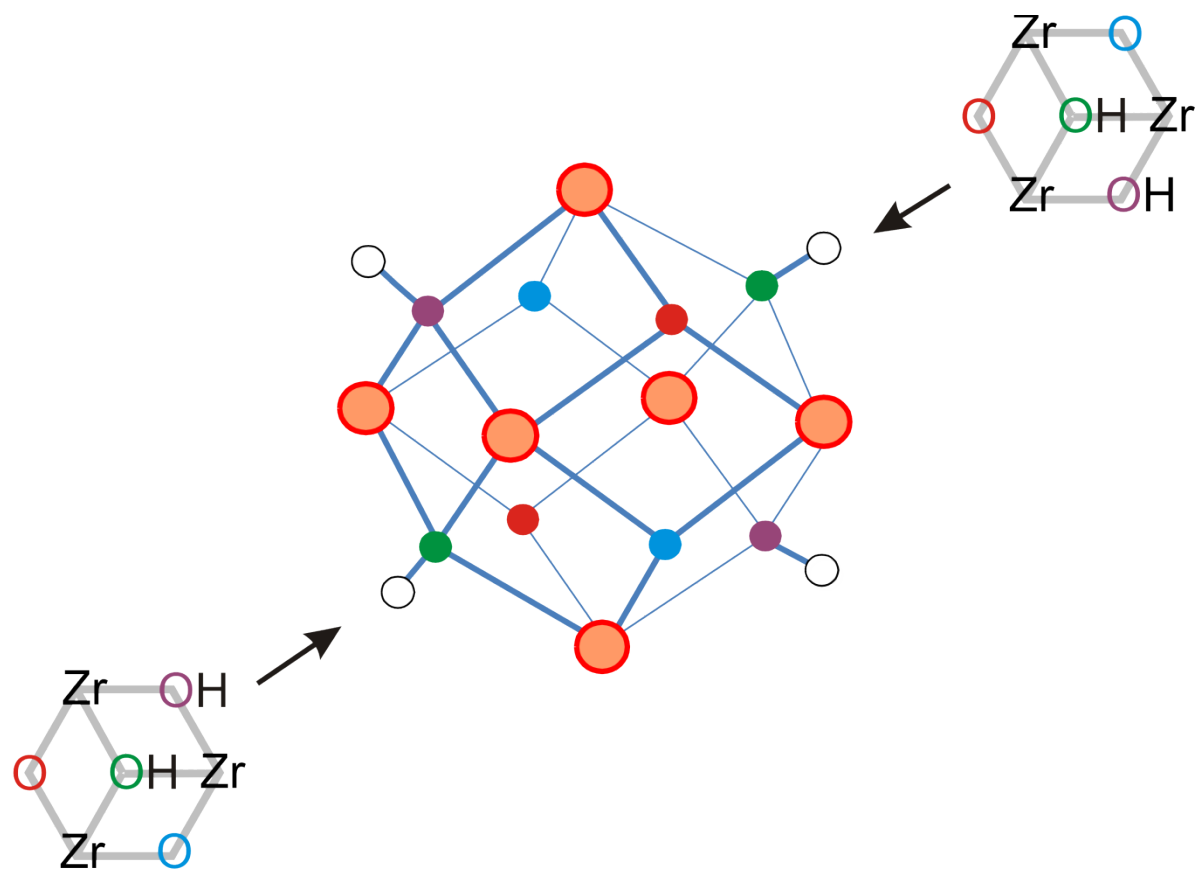


Figure S2: Position of the hydrogens lies on one rectangle, in one plane. The representations for different viewpoints (black arrows) are given.

2. Computational Methodology: static periodic calculations

We studied the synthesis (130 °C and 1 bar) and activation pretreatment (320 °C and 10^{-3} mbar) of UiO-66 on different unit cells with periodic DFT-D calculations. Periodic DFT-D calculations are performed with the Vienna Ab Initio Simulation Package (VASP 5.2.12)¹⁻⁴. The unit cell of all structures is first optimized with a plane wave kinetic energy cutoff of 600 eV, employing the PBE exchange-correlation functional^{5, 6} with D3-dispersion corrections according to Grimme⁷. Furthermore, the energy cut off for structural optimizations is lowered to 400 eV. The energy refinements and frequency calculations have been performed on the PBE-D3 level of theory, including Becke–Johnson damping⁸. The projector augmented wave approximation (PAW)⁹ is used and Brillouin zone sampling is restricted to the Γ -point. Gaussian smearing² is applied to improve convergence: 0.05 eV for cell optimizations, 0.02 eV for the subsequent energy and frequency calculations at PBE-D3 with Becke Jones damping⁸. Additionally, the convergence criterion for the electronic self-consistent field (SCF) problem is set to 10^{-5} eV. Remark that in this paper, we increased the amount of atoms that is taken up in the partial Hessian calculations (see **Figure S.3**), while previously we opted for the minimal selection of atoms, which was different for each reaction step¹⁰. Together with a reduced plane wave basis set (400 eV), this explains why energy differences are quantitatively changed from the values that were published earlier¹⁰.

All geometries are built with ZEOBUILDER¹¹ from the crystallographic information file provided by Cavka et al.¹². In order to have free-energy differences between reactants and products, a relevant partial Hessian vibrational analysis (PHVA) is determined (only the part that changes most in reactants and products is selected and the rest of the atoms is thus considered fixed, this part is shown in Figures 1, 2 and 3 in the main paper and in Figure S.3). The PHVA method¹³⁻¹⁷ is well known in the literature and has been previously applied to study kinetics¹⁸⁻²⁰. The numerical partial Hessian is calculated by displacements in a , b and c -axis of ± 0.015 Å, while the vibrational modes are extracted using the normal mode analysis as implemented in the in-house developed post-processing toolkit TAMKIN²¹. In one case (structure J, **Figure S.4** and **S.5**), we found a small imaginary frequency, which was substituted by 50 cm^{-1} for the thermoanalysis.

In **Figure S.3**, the unit cell of the parent periodic UiO-66 structure¹² comprises: $\langle \text{Zr}_6\text{O}_4(\text{OH})_4(\text{bdc})_6 \rangle_4$, where bdc stands for benzene dicarboxylate or terephthalic acid. For convenience the notation RCOO^- is introduced representing a half of bdc linker. TFA is short for trifluoroacetic acid CF_3COOH . 4 carboxylate oxygen atoms are bound to each Zr atom. With one TFA and defect site incorporated per unit cell, the UiO-66-TFA unit cell is composed of $\langle \text{Zr}_6\text{O}_4(\text{OH})_4(\text{RCOO})_{11}(\text{CF}_3\text{COO}) \rangle \langle \text{Zr}_6\text{O}_5(\text{OH})_3(\text{RCOO})_{11} \rangle \langle \text{Zr}_6\text{O}_4(\text{OH})_4(\text{RCOO})_{12} \rangle_2$.

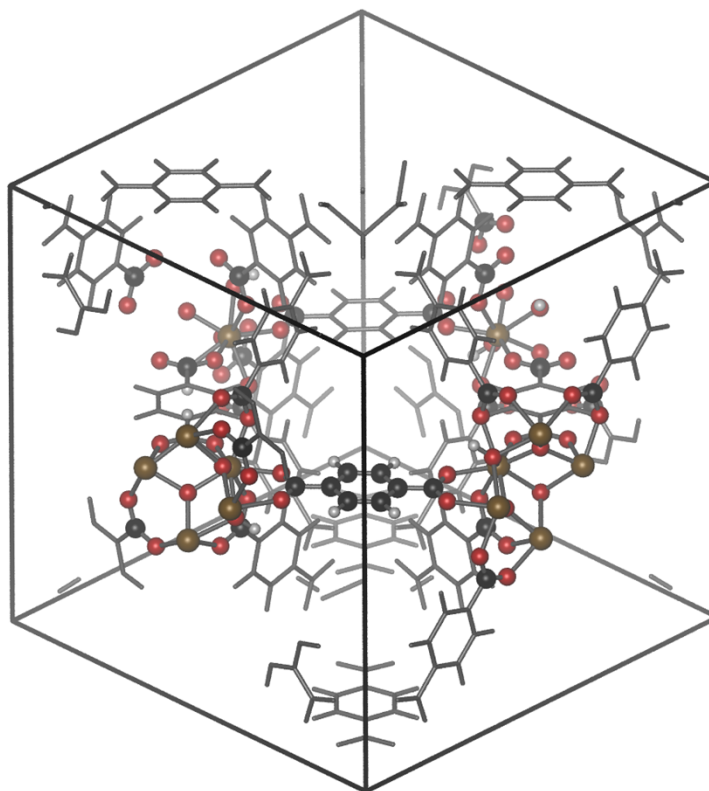


Figure S.3: Structure A of the main paper – with unit cell formula $\langle \text{Zr}_6\text{O}_4(\text{OH})_4(\text{RCOO})_6 \rangle_4$ – is represented. The part of the framework that is included in the partial hessian calculations is made visible as colored balls.

In case of only 1 linker deficiency in a unit cell with 4 $\text{Zr}_6\text{O}_4(\text{OH})_4$ bricks, the structures are quite rigid and the volume of these structure does not change much from that of structure A (no missing linkers), see **Table S.1**. Therefore, we decided to omit cell optimization for structures N, E and M.

Table S.1: Optimized unit cell volumes (\AA^3) for all structures.

unit cell was cell optimized for;	Volume (\AA^3)	Structures with the same cell parameters (unit cell was not optimized)
A X(BDC)	9111.5	
B X(TFA)	9091.6	N X(TFA,HCl)
C X(2TFA)	9097.5	
D X(2H ₂ O)	9125.5	E X(2HCl)
F X ^{H2O1} (BDC)	9098.4	
G X(0)	9091.2	M Y(2HCl)
H X ^{H2O1} (TFA)	9061.3	
I X ^{2H2O1} (BDC)	9087.6	
J X ^{2H2O1} (TFA)	9066.2	
K X ^{H2O1} (0)	9060.3	
L Y(BDC)	9111.5	

4. Figure S.5: Overview of reactions during post-synthesis activation.

legend:

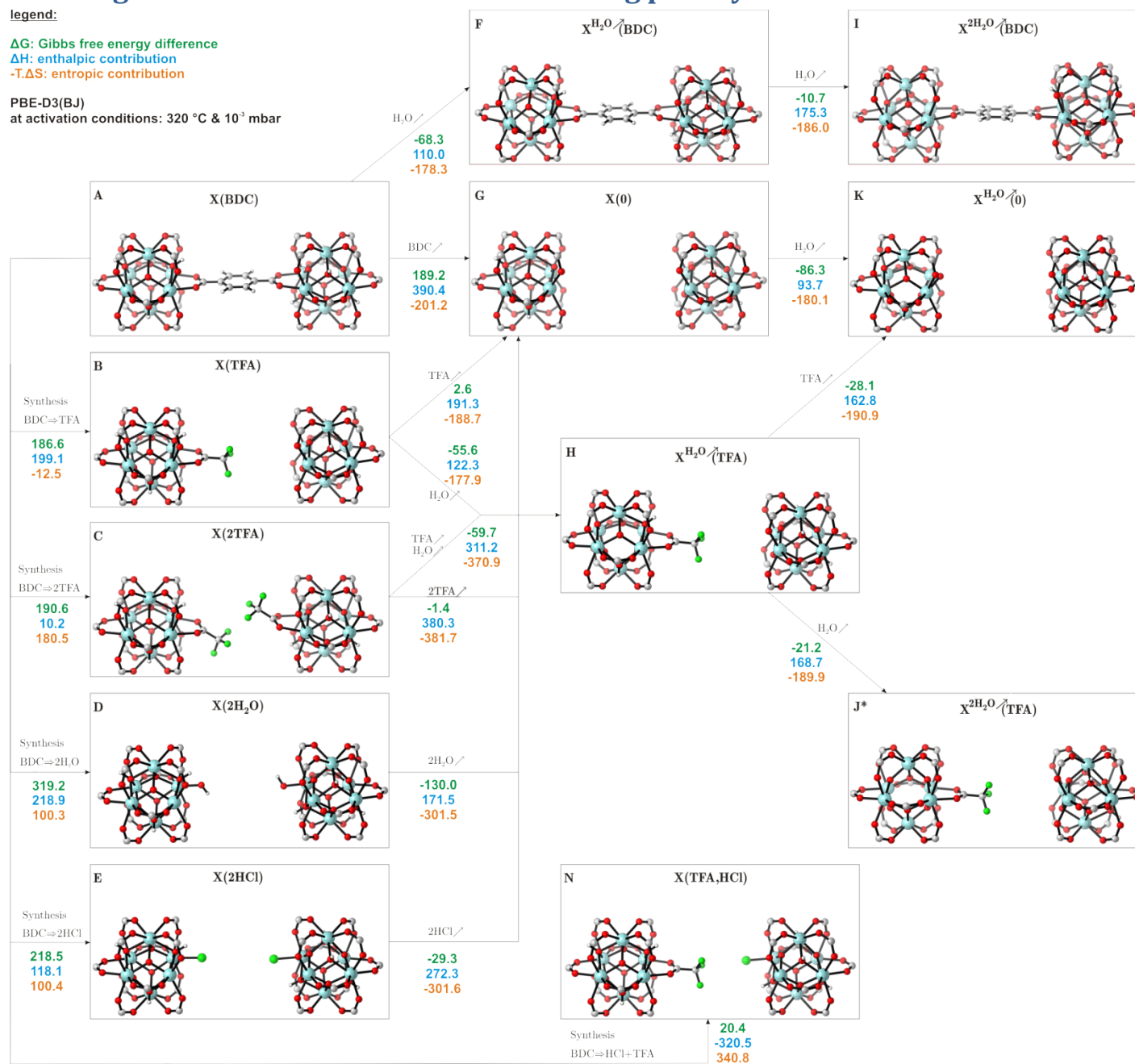
ΔG : Gibbs free energy difference

ΔH : enthalpic contribution

$-T\Delta S$: entropic contribution

PBE-D3(BJ)

at activation conditions: 320 °C & 10³ mbar



5. Computational Methodology: Periodic Molecular Dynamics simulations and Nudged Elastic Band calculations to unravel reaction path for dehydroxylation.

To study the dehydroxylation behavior of the $Zr_6O_4(OH)_4$ inorganic bricks of the UiO-66 type materials, ab initio molecular dynamics (AIMD) simulations are performed by means of density functional theory (DFT) calculations in a fully periodic UiO-66 catalyst models with unit cell formulas $[Zr_6O_5(OH)_3(RCOO)_{11/2}]_2$ $[Zr_6O_4(OH)_4(RCOO)_{12}]_2$ (large model) and $Zr_6O_6(OH)_2(RCOO)_{10}Zr_6O_4(OH)_4(RCOO)_{12}$ (small model). Both structures exhibit one missing BDC linker, which – in case of the small model - leads to topology with straight parallelogram shaped channels throughout the material (pore size ~ 10 - 11 Å). AIMD simulations were performed with the CP2K simulation package²² on the DFT level of theory and with Gaussian Plane Wave basis sets (GPW)^{23, 24}. The BLYP functional^{25, 26} with the DZVP-GTH basis set²⁷ was chosen, including Grimme D3 dispersion corrections⁷. The time step for integration of the equations of motion was set to 0.5 fs.

The large model system was equilibrated at 373 K and 10^{-9} bar in the NPT ensemble, followed by equilibration steps until the temperature was converged. For constant temperature the Nosé–Hoover thermostat has been used as one of the most accurate and efficient. The barostat has been selected to preserve changes in pressure. The temperature was systematically increased by 100 K and the effects on the structure were investigated by visualization of the obtained trajectory. At a temperature of 1273 K, we observed simultaneous decooordination of the μ_3 -OH and one of the neighbouring terephthalates. Based on this simulation, a decoordinated state was constructed for the small model, which was further cell optimized using VASP with the PBE-D3(BJ) employing a kinetic energy cut off of 600 eV (similar computational procedure as in **Section 2**), yielding structure **18**. Between the unperturbed system **0**, and structure **18**, with one intermediate structure **9** was arbitrarily constructed, on the basis of initial Nudged Elastic Band (NEB) simulations²⁸. Then, two NEB simulations (NEB1, NEB2) – each with eight images – are performed with varying cell parameters were performed to estimate the **intermediate structures 1-8** and **10-17**. By looking at the energy profiles of the NEB simulation, we saw that the local minimum corresponding with structure 9 –where one terephthalate was fully decoordinated could be avoided. We decided to omit structure 9 and divided the sequence of structures between 0 and 18 into three different NEBs (NEBa, NEBb, NEBc). Therefore, we first reoptimized structure **6** and **12** again with a small optimization step size (POTIM=0.1) to prevent an escape from these local minima on the potential energy surface. After running the three new NEBs, (between **0** and **6**, **6** and **12**, **12** and **18**), we obtained slightly different intermediate structures (**1-5**, **7-11**, **13-17**).

From structure **18**, the species after water removal was arbitrarily constructed using Zeobuilder¹¹ (structure **27**), optimized and then a NEB was performed to construct the intermediate structures **19-26**. Afterwards, all energies were refined at PBE-D3(BJ) employing a kinetic energy cut off of 400 eV in combination with an energetic convergence criterion for the SCF of 10^{-8} eV.

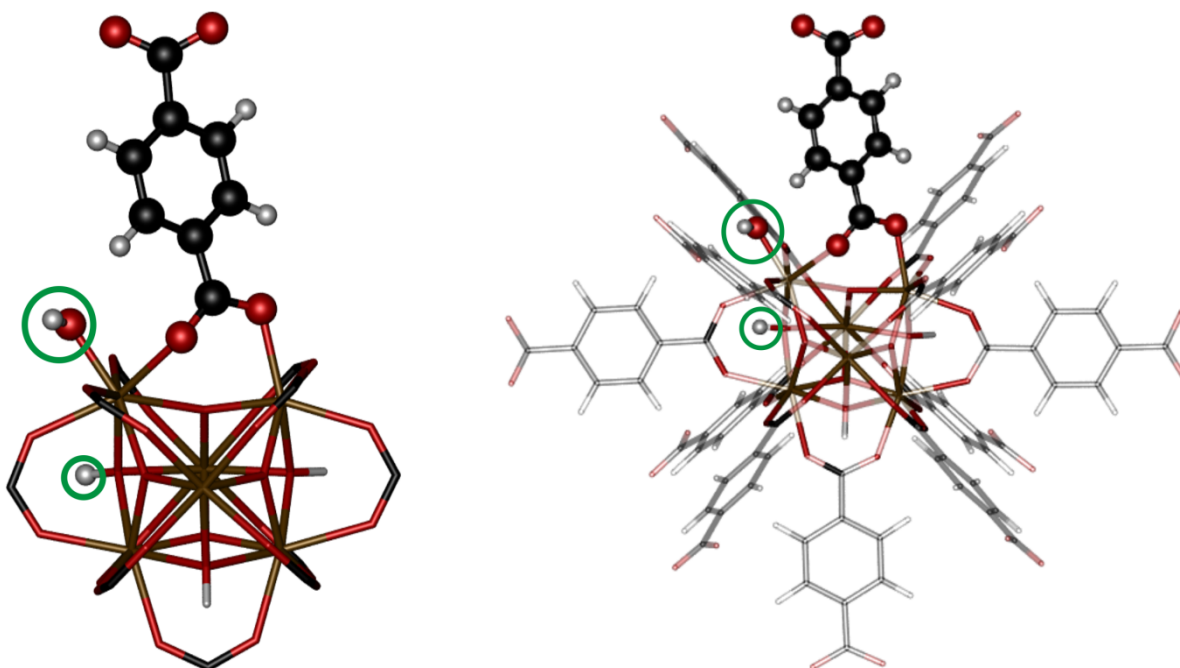


Figure S.6. Structure 18 of the NEB. The relevant atoms leading to the final removal of water are encircled. The linkers, which are not involved in the dehydroxylation, are omitted (left) or given in the shadow (right), to keep the transparency of the figure.

6. Computational Methodology: Cluster Calculations

All clusters used in this paper were constructed based on the clusters used in an earlier paper by Vermoortele and Vandichel et al.²⁹. An overview of the clusters is given together with the pre-transition state reactants, transition state and post-TS products in **Figure S.7**. The enthalpy and entropy contributions to the free energies are given in **Table S.2**. Additionally, we include information of cluster models where we removed one of the two terephthalates (**Figure S.8**, **Figure S.9** and **Table S.3**).

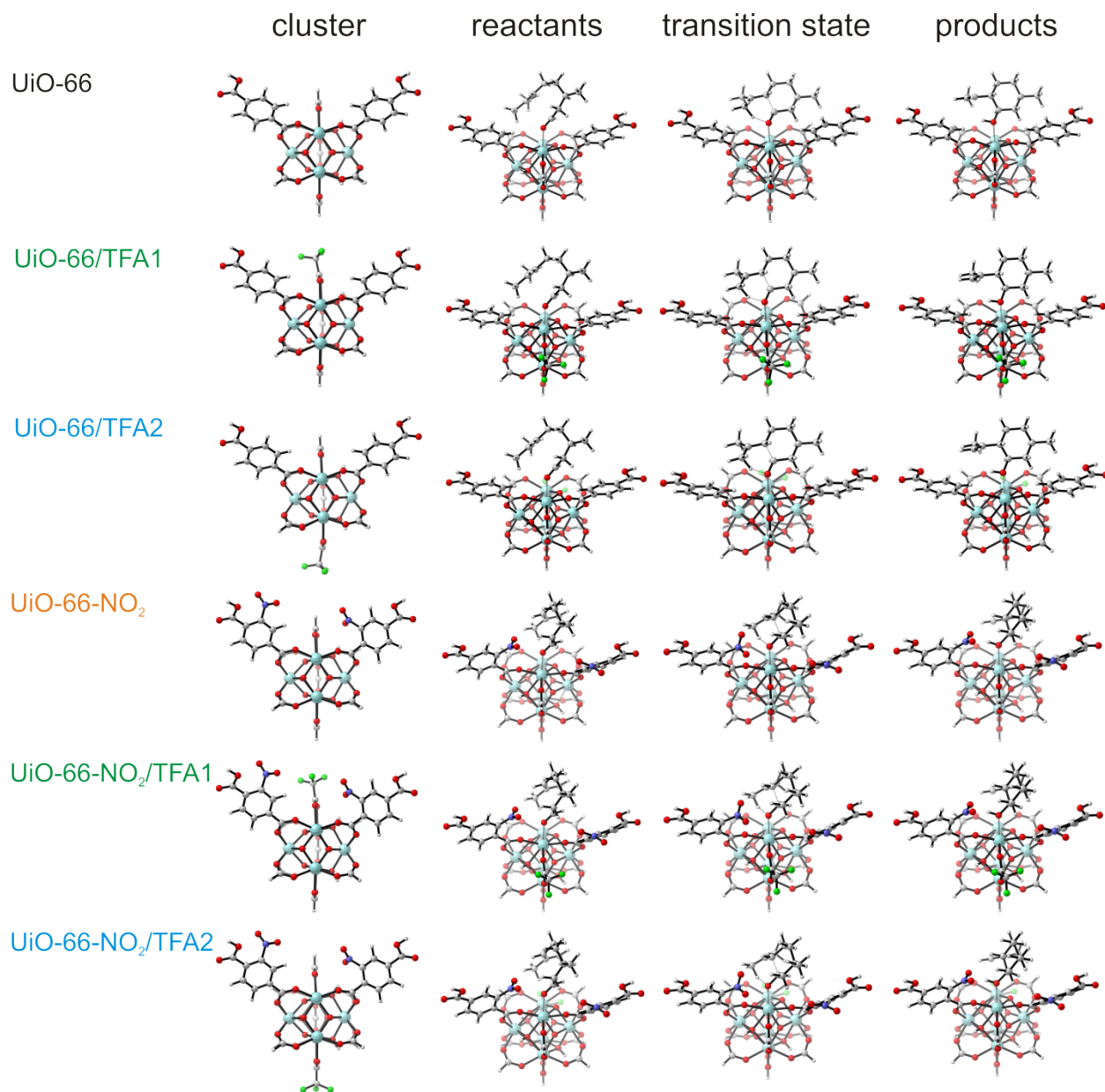


Figure S.7. Extended cluster models used in the paper, together with reactants, transition states and products for the citronellal cyclization. The terephthalic linkers closest to the active site are maintained. Free energy profile can be found in **Figure 6** of the main paper.

Geometry optimizations were performed with the Gaussian09 package³⁰ using the B3LYP hybrid functional^{31, 32}. The double-zeta Pople basis set 4-31g* was used for all atoms except for Zr, for which the LANL2DZ effective core potential and basis set were applied³³. Afterwards single point energy refinements at the B3LYP/6-31+g(d) level of theory were performed to account for the electronic energy effects of the substituents on the terephthalate linkers, maintaining the LANL2DZ effective core potential and basis set for Zr. Furthermore, van der Waals corrections in conjunction with the B3LYP functional as developed by Grimme³⁴ were computed. In this paper, the D3-version⁷ of the dispersion

corrections was calculated using the program distributed by Grimme. Starting from transition state geometries, the quasi-IRC approach allowed to locate the product geometries. In the quasi-IRC approach, the geometry of the transition state is slightly perturbed in the direction of the reactants and products followed by full geometry optimizations. The PHVA method^{13, 14, 16}, applied also previously for kinetics²⁰, was then used to investigate the kinetics of the citronellal cyclization on the extended UiO-66 clusters. The substituted clusters were constructed by adding the substituent groups onto the parent UiO-66 cluster.

Table S.2. Kinetic data for the citronellal cyclization to isopulegol at 373 K (nomenclature clusters in **Figure S.7**). Free energy, enthalpy and entropy contributions in the adsorbed state (ads) and in the transition state (\ddagger) (kJ/mol). The rate constants (k_{373}^{fwd}) are given in units of $\text{m}^3 \cdot \text{mol}^{-1} \cdot \text{s}^{-1}$ for the apparent kinetics and in s^{-1} for the intrinsic kinetics. The relative rates versus UiO-66 model are also given.

Pre-TS	ΔG_{373}^{ads}	ΔH_{373}^{ads}	$-T \cdot \Delta S_{373}^{ads}$	
UiO-66*	-15.7	-88.6	72.9	
UiO-66/TFA1	-19.4	-93.0	73.6	
UiO-66/TFA2	-18.7	-92.2	73.5	
UiO-66-NO ₂ *	-23.7	-104	80.4	
UiO-66-NO ₂ /TFA1	-30.3	-109.6	79.3	
UiO-66-NO ₂ /TFA2	-26.6	-107.5	80.8	
cluster(g) + citronellal(g) → TS	$\Delta G_{373}^{\ddagger}$	$\Delta H_{373}^{\ddagger}$	$-T \cdot \Delta S_{373}^{\ddagger}$	k_{373}^{fwd}
UiO-66*	56.4	-44.2	100.6	3.03E+03 (1.0)
UiO-66/TFA1	51.5	-49.2	100.6	1.49E+04 (4.9)
UiO-66/TFA2	52.0	-49.1	101.1	1.24E+04 (4.1)
UiO-66-NO ₂ *	37.4	-67.8	105.2	1.40E+06 (463.3)
UiO-66-NO ₂ /TFA1	32.8	-72.8	105.5	6.18E+06 (2039.1)
UiO-66-NO ₂ /TFA2	32.1	-71.6	103.7	7.79E+06 (2572.1)
Cluster---citronellal(ads) → TS	$\Delta G_{373}^{\ddagger}$	$\Delta H_{373}^{\ddagger}$	$-T \cdot \Delta S_{373}^{\ddagger}$	k_{373}^{fwd}
UiO-66*	72.1	44.4	27.8	6.15E+02 (1.0)
UiO-66/TFA1	70.9	43.8	27.0	9.28E+02 (1.5)
UiO-66/TFA2	70.7	43.1	27.6	9.72E+02 (1.6)
UiO-66-NO ₂ *	61.1	36.4	24.7	2.17E+04 (35.4)
UiO-66-NO ₂ /TFA1	63.1	36.8	26.3	1.13E+04 (18.4)
UiO-66-NO ₂ /TFA2	58.7	35.8	22.9	4.68E+04 (76.2)
*data taken from ref. ²⁹				

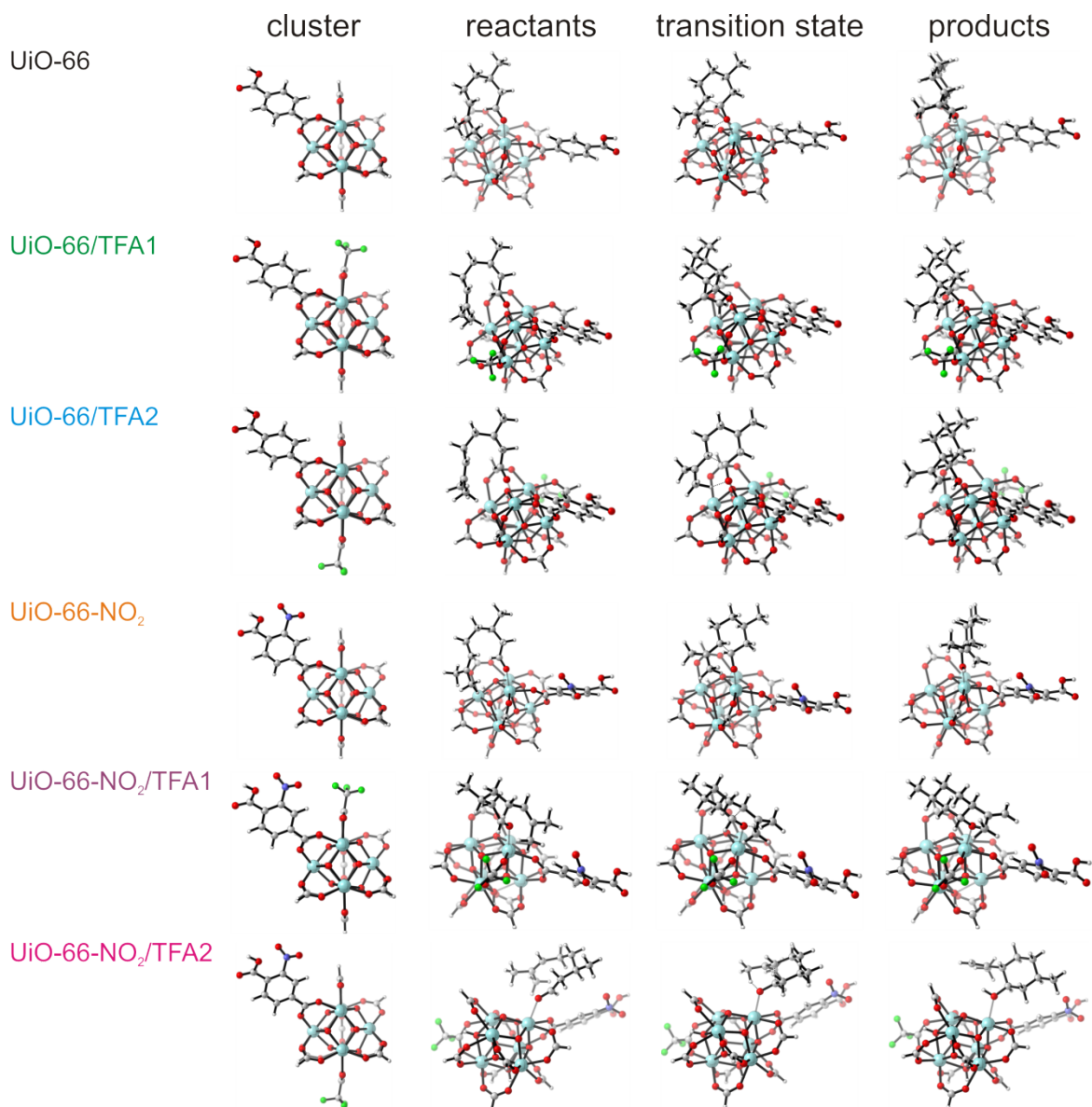


Figure S.8. Extended cluster models used in the paper, together with reactants, transition states and products for the citronellal cyclization. The terephthalic linkers closest to the active site are maintained. Free energy profiles can be found in **Figure S.9**.

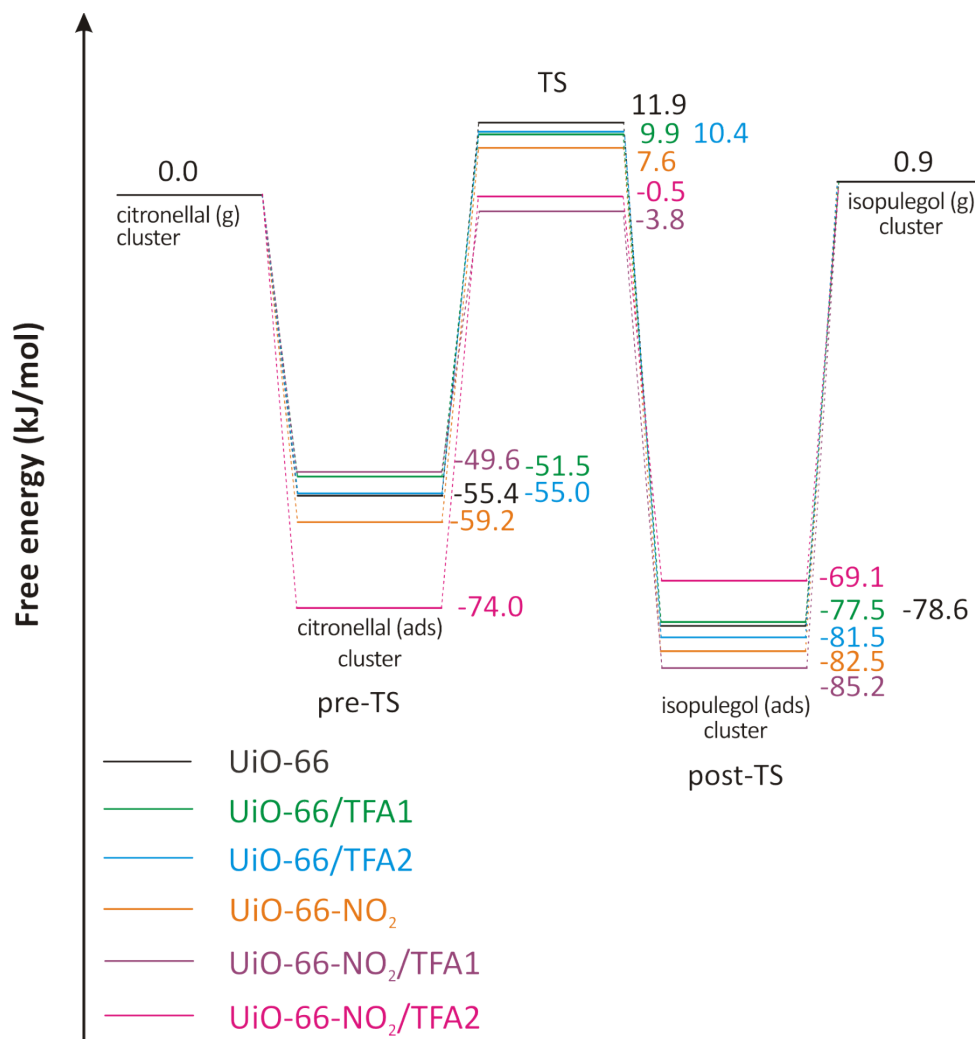


Figure S.9. Free-energy profiles, calculated at 373 K, for citronellal cyclization to isopulegol on extended cluster models where one extra linker was removed (**Figure S.8**).

Table S.3: Kinetic data for the citronellal cyclization to isopulegol at 373 K (nomenclature clusters in **Figure S.8**). Free energy, enthalpy and entropy contributions in the adsorbed state (ads) and in the transition state (\ddagger) (kJ/mol). The rate constants (k_{373}^{fwd}) are given in units of $\text{m}^3 \cdot \text{mol}^{-1} \cdot \text{s}^{-1}$ for the apparent kinetics and in s^{-1} for the intrinsic kinetics. The relative rates of UiO-66-NO₂-TFA, UiO-66-NO₂ versus UiO-

Pre-TS	ΔG_{373}^{ads}	ΔH_{373}^{ads}	$-T \cdot \Delta S_{373}^{ads}$	
UiO-66*	-55.4	-125.5	70.1	
UiO-66/TFA1	-51.5	-129.1	77.6	
UiO-66/TFA2	-55.0	-126.4	71.4	
UiO-66-NO ₂ *	-59.2	-130.3	71.1	
UiO-66-NO ₂ /TFA1	-49.6	-139.8	90.2	
UiO-66-NO ₂ /TFA2	-74.0	-148.8	74.8	
cluster(g) + citronellal(g) → TS	$\Delta G_{373}^{\ddagger}$	$\Delta H_{373}^{\ddagger}$	$-T \cdot \Delta S_{373}^{\ddagger}$	k_{373}^{fwd}
UiO-66*	11.9	-79.5	91.5	5.17E+09 (1.0)
UiO-66/TFA1	9.9	-91.6	101.5	1.00E+10 (1.9)
UiO-66/TFA2	10.4	-80.6	90.9	8.55E+09 (1.7)
UiO-66-NO ₂ *	7.6	-80.7	88.3	2.09E+10 (4.0)
UiO-66-NO ₂ /TFA1	-3.8	-110.9	107.1	8.24E+11 (159.3)
UiO-66-NO ₂ /TFA2	-0.5	-97.4	96.9	2.84E+11 (54.9)
Cluster---citronellal(ads) → TS	$\Delta G_{373}^{\ddagger}$	$\Delta H_{373}^{\ddagger}$	$-T \cdot \Delta S_{373}^{\ddagger}$	k_{373}^{fwd}
UiO-66*	67.3	46.0	21.3	2.90E+03 (1.0)
UiO-66/TFA1	61.4	37.5	23.8	1.98E+04 (6.8)
UiO-66/TFA2	65.4	45.8	19.5	5.47E+03 (1.9)
UiO-66-NO ₂ *	66.8	49.6	17.2	3.42E+03 (1.2)
UiO-66-NO ₂ /TFA1	45.8	28.8	16.9	3.04E+06 (1047.2)
UiO-66-NO ₂ /TFA2	73.5	51.4	22.1	4.0E+02 (0.14)

*data taken from ref. ²⁹

66 are also given.

7. Computational Methodology: extended Hirshfeld-e charges

Hirshfeld-e partial charges³⁵ were computed using the Horton program (T. Verstraelen, S. Vandenbrande, M. Chan, F. H. Zadeh, C. González, P. A. Limacher, A. Malek; Horton 1.2.1, <http://theochem.github.com/horton/>, 2013). The correlation of the extended Hirshfeld charges with activation enthalpy for the citronellal cyclization is shown in **Figure S.7**. Note that the correlation between the apparent enthalpy and the Hirshfeld-e charges is the greatest.

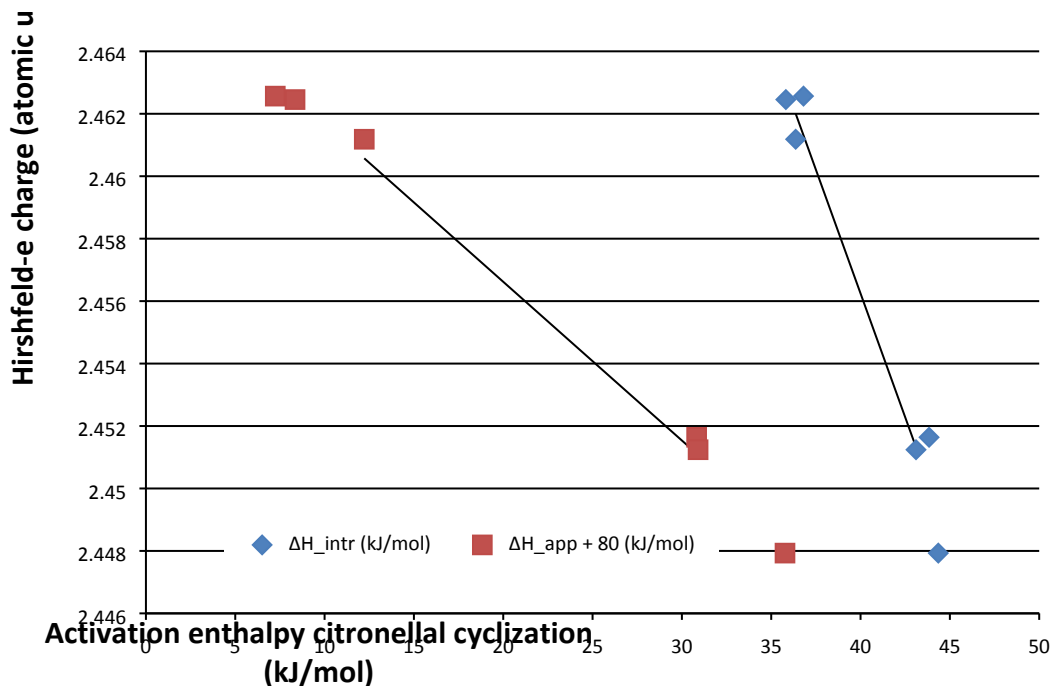


Figure S.10. Plot of the Hirshfeld-e charge on the active Zr atom (calculated on an empty cluster model) in relation to the activation enthalpy ΔH (kJ/mol). The enthalpy difference between gas phase reactants and transition state is given as ΔH_{app} , while the enthalpy difference between adsorbed reactants and the transition state is indicated as ΔH_{intr} . Hirshfeld-e charges were computed at the level of theory of the energy refinements B3LYP/6-31+g(d).

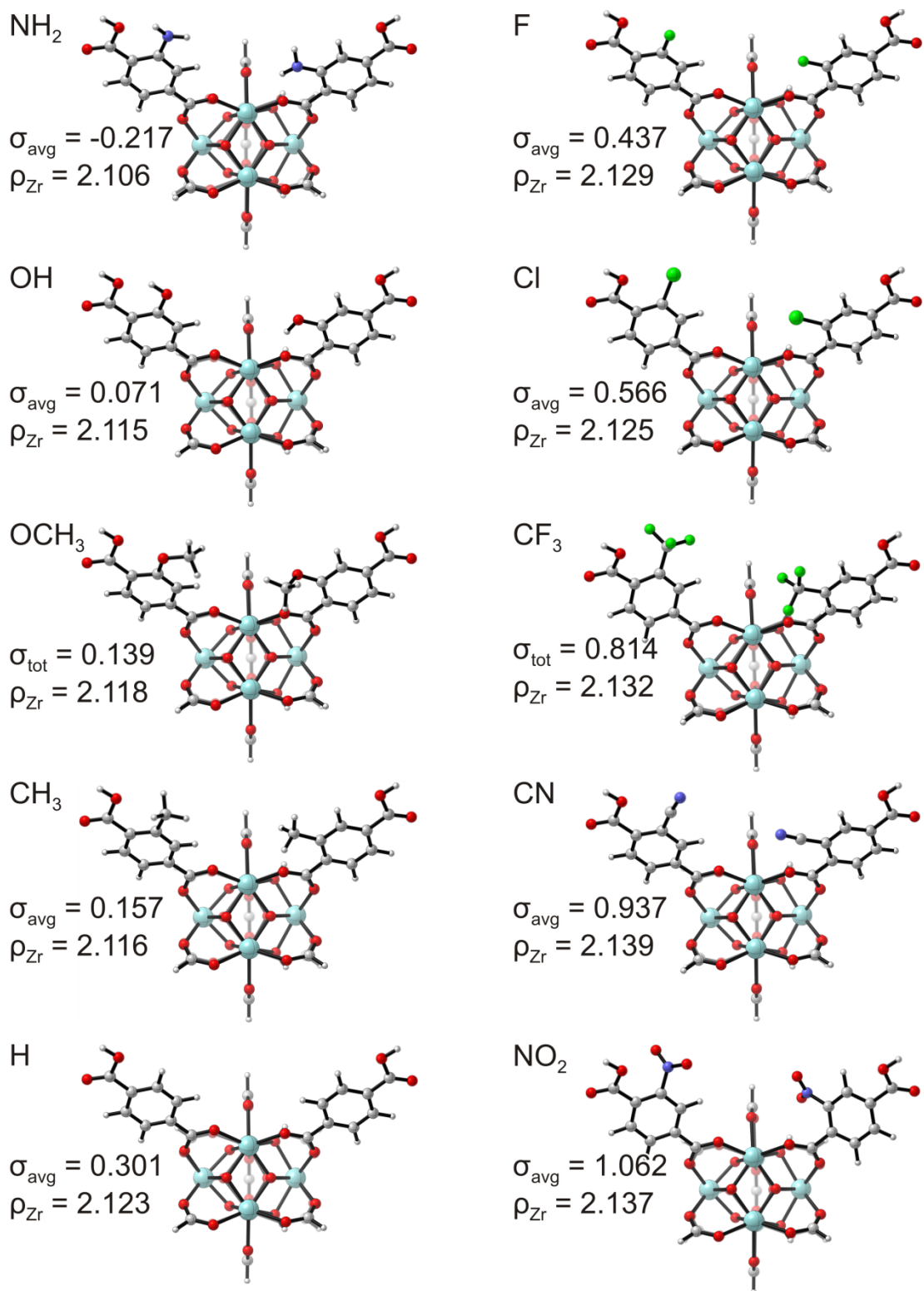


Figure S.11. All investigated cluster models with the average experimental σ_{avg} value ($=\log(10^{\sigma_{\text{m}}}) + 10^{\sigma_{\text{p}}}$) and the Hirshfeld-e charge ρ_{Zr} at B3LYP/Def2TZVPP.

References:

1. G. Kresse and J. Furthmuller, *Physical Review B*, 1996, **54**, 11169.
2. G. Kresse and J. Furthmuller, *Computational Materials Science*, 1996, **6**, 15-50.
3. G. Kresse and J. Hafner, *Physical Review B*, 1993, **47**, 558.
4. G. Kresse and J. Hafner, *Physical Review B*, 1994, **49**, 14251.
5. J. P. Perdew, K. Burke and M. Ernzerhof, *Physical Review Letters*, 1996, **77**, 3865.
6. J. P. Perdew, K. Burke and M. Ernzerhof, *Physical Review Letters*, 1997, **78**, 1396.
7. S. Grimme, J. Antony, S. Ehrlich and H. Krieg, *J Chem Phys*, 2010, **132**.
8. S. Grimme, S. Ehrlich and L. Goerigk, *J Comput Chem*, 2011, **32**, 1456-1465.
9. P. E. Blochl, *Physical Review B*, 1994, **50**, 17953.
10. F. Vermoortele, B. Bueken, G. Le Bars, B. Van de Voorde, M. Vandichel, K. Houthoofd, A. Vimont, M. Daturi, M. Waroquier, V. Van Speybroeck, C. Kirschhock and D. E. De Vos, *J Am Chem Soc*, 2013, **135**, 11465-11468.
11. T. Verstraelen, V. Van Speybroeck and M. Waroquier, *J Chem Inf Model*, 2008, **48**, 1530-1541.
12. J. H. Cavka, S. Jakobsen, U. Olsbye, N. Guillou, C. Lamberti, S. Bordiga and K. P. Lillerud, *J Am Chem Soc*, 2008, **130**, 13850-13851.
13. A. Ghysels, V. Van Speybroeck, T. Verstraelen, D. Van Neck and M. Waroquier, *J. Chem. Theory Comput.*, 2008, **4**, 614-625.
14. A. Ghysels, V. Van Speybroeck, E. Pauwels, D. Van Neck, B. R. Brooks and M. Waroquier, *J. Chem. Theory Comput.*, 2009, **5**, 1203-1215.
15. A. Ghysels, V. Van Speybroeck, E. Pauwels, S. Catak, B. R. Brooks, D. Van Neck and M. Waroquier, *Journal of Computational Chemistry*, 2009, submitted.
16. A. Ghysels, D. Van Neck and M. Waroquier, *J. Chem. Phys.*, 2007, **127**, 164108.
17. A. Ghysels, D. Van Neck, V. Van Speybroeck, T. Verstraelen and M. Waroquier, *Journal of Chemical Physics*, 2007, **126**, 224102.
18. D. Lesthaeghe, J. Van der Mynsbrugge, M. Vandichel, M. Waroquier and V. Van Speybroeck, *ChemCatChem*, 2011, **3**, 208-212.
19. V. Van Speybroeck, J. Van der Mynsbrugge, M. Vandichel, K. Hemelsoet, D. Lesthaeghe, A. Ghysels, G. B. Marin and M. Waroquier, *J. Am. Chem. Soc.*, 2011, **133**, 888-899.
20. M. Vandichel, D. Lesthaeghe, J. Van der Mynsbrugge, M. Waroquier and V. Van Speybroeck, *Journal of Catalysis*, 2010, **271**, 67-78.
21. A. Ghysels, T. Verstraelen, K. Hemelsoet, M. Waroquier and V. Van Speybroeck, *J Chem Inf Model*, 2010, **50**, 1736-1750.
22. J. VandeVondele, M. Krack, F. Mohamed, M. Parrinello, T. Chassaing and J. Hutter, *Comput. Phys. Commun.*, 2005, **167**, 103-128.
23. G. Lippert, J. Hutter and M. Parrinello, *Theor Chem Acc*, 1999, **103**, 124-140.
24. G. Lippert, J. Hutter and M. Parrinello, *Mol. Phys.*, 1997, **92**, 477-487.
25. C. Lee, W. Yang and R. G. Parr, *Phys Rev B*, 1988, **37**, 785-789.
26. A. D. Becke, *Physical Review A*, 1988, **38**, 3098-3100.
27. S. Goedecker, M. Teter and J. Hutter, *Phys Rev B*, 1996, **54**, 1703-1710.
28. G. Henkelman, B. P. Uberuaga and H. Jónsson, *The Journal of Chemical Physics*, 2000, **113**, 9901-9904.
29. F. Vermoortele, M. Vandichel, B. Van de Voorde, R. Ameloot, M. Waroquier, V. Van Speybroeck and D. E. De Vos, *Angew Chem Int Edit*, 2012, **51**, 4887-4890.
30. M. P. Suh, H. J. Park, T. K. Prasad and D.-W. Lim, *Chem Rev*, 2012, **112**, 782-835.

31. A. D. Becke, *J. Chem. Phys.*, 1993, **98**, 5648-5652.
32. C. T. Lee, W. T. Yang and R. G. Parr, *Physical Review B*, 1988, **37**, 785-789.
33. P. J. Hay and W. R. Wadt, *J. Chem. Phys.*, 1985, **82**, 270-283.
34. S. Grimme, *J Comput Chem*, 2004, **25**, 1463-1473.
35. T. Verstraelen, P. W. Ayers, V. Van Speybroeck and M. Waroquier, *Journal of Chemical Theory and Computation*, 2013, **9**, 2221-2225.